Modeling dynamic stall of an airfoil with vortex generators using a double-wake panel model with viscous–inviscid interaction

Yu, Wei; Bajarūnas, Lukas K.; Zanon, Alessandro; Ferreira, Carlos J.S.

Citation (APA)
Yu, W., Bajarūnas, L. K., Zanon, A., & Ferreira, C. J. S. (2024). Modeling dynamic stall of an airfoil with vortex generators using a double-wake panel model with viscous–inviscid interaction. *Wind Energy*, *27*(3), 277-297. https://doi.org/10.1002/we.2889

Important note
To cite this publication, please use the final published version (if applicable).
Please check the document version above.

WILEY

Modeling dynamic stall of an airfoil with vortex generators using a double-wake panel model with viscous–inviscid interaction

Wei Yu[1] 🟢　│　Lukas K. Bajarūnas[1]　│　Alessandro Zanon[2]　│　Carlos J. S. Ferreira[1]

[1]Faculty of Aerospace Engineering, Delft University of Technology, Delft, The Netherlands

[2]Center for Low-Emission Transport, AIT Austrian Institute of Technology GmbH, Vienna, Austria

Correspondence
Wei Yu, Faculty of Aerospace Engineering, Delft University of Technology, Kluyverweg 1, 2629 HS, Delft, The Netherlands.
Email: W.Yu@tudelft.nl

Abstract

Vortex generators (VGs) have been widely applied to wind turbines thanks to their potential to increase aerodynamic performance. Due to the complex inflow perceived by a rotor and the proneness to flow separation, VGs on wind turbines usually experience highly unsteady flow. While there are models that exist to simulate the steady effects of VGs, we lack a fast and efficient tool to model the unsteady performance of airfoils equipped with VGs. This paper adopts an unsteady double-wake panel model with viscous–inviscid interaction developed to simulate a vertical axis turbine in dynamic stall, adding the capability of predicting the dynamic aerodynamic performance of VG-equipped airfoils. The results of a series of steady and unsteady cases of an airfoil with different VG configurations in various pitch motions in free and forced transition are verified against experimental data. Results show that the double wake model offers results with sufficient accuracy compared with experimental data to claim the model's validity in a preliminary evaluation of an airfoil's capability to prevent stall with VGs. A few limitations, including the accuracy in prediction the transition location, separation, and reattachment, have been identified for future development.

KEYWORDS
double wake, dynamic stall, viscous–inviscid interaction, vortex generators, vortex panel method

1 │ INTRODUCTION

Vortex generators (VGs) are passive flow control devices widespread in the aerospace and energy industries. The primary purpose of applying VGs on wind turbines is to limit the separation of flows at the inboard region, which usually experiences thick sectional surfaces and high angles of attack.[1] While the need to compensate for the wind turbine performance loss caused by blade surface degradation[2] and to control dynamic stall[3,4] drives it to move more outboard.

VGs have been extensively studied since their first proposal.[5] Schubauer and Spangenberg[6] experimented on a few possible VG designs for forced mixing in the boundary layer. Pearcey[7] investigated VG layouts for vane-type generators to prevent shock-induced separation. Lögdberg

et al[8] studied the streamwise evolution of longitudinal vortices. Godard and Stanislas[9] shed some insight on VG configurations, such as the VG shapes, rotation direction, aspect ratio, and skew angles. Different VG configurations were also tested for wind applications.[1,10] However, the studies mentioned above focus on a steady flow.

Wind turbines experience highly unsteady flow due to the rotation, the instantaneous variation in wind speed and direction, the fluid–structure interaction of the flexible blade of current large-scale wind turbines, and control deployment. Under these circumstances, dynamic stall tends to occur. Dynamic stall is an event that leads to dynamic delays of stall of a moving airfoil when the static stall angle is exceeded.[11] Four stages characterize the dynamic stall[12]: flow reversals within the boundary layer when the airfoil exceed the static stall angle; vortices detach and convect over the airfoil surface, which induces extra lift; full separation starts when the vortex reaches the trailing edge; and reattachment from front to back when angles of attack are reduced. The periodic loading resulting from dynamic stall leads to increased fatigue load on wind turbine blades and thus reduces their lifespan.[13] Due to the constantly varying angle of attack, dynamic stall is of vital importance in the aerodynamics of vertical axis wind turbines (VAWTs).[14–18]

The use of VG to limit dynamic stall has also been studied experimentally. Carr and Mcalister[19] found that a slat placed at the leading edge could suppress the dynamic stall phenomenon. Choudhry et al[20] discovered that VG-induced counter-rotating vortices could break up the large dynamic stall vortex, thus reducing the strength of the dynamic stall vortex. Mai[3] concluded that the leading-edge VG could increase the overall lift of a rotorcraft airfoil by disturbing the dynamic stall vortex. Le Pape et al[21] further discovered that the VG height plays a more influential role in breaking up dynamic stall vortices. The recently published dataset[22] measured the steady and unsteady aerodynamic performance of wind turbine airfoils equipped with different VG configurations in various pitch motions, which will be used for the validation of the developed model in this paper.

VGs are designed using experimental tests as well as numerical modeling. Due to the cost of the former in the iterative design process, we need capable modeling techniques to provide a design direction or optimize the VGs configurations. Most numerical studies on VGs are computational fluid dynamics (CFD) based in direct or indirect ways; namely, full geometry is resolved or represents the effect of VGs by changing flow features. The work on fully resolved CFD on VGs includes.[23–25] However, due to the small length scale of VGs, fully resolved CFDs is also costly. Methods are proposed to model VG by accounting for the impact on the flow features without considering the exact geometry. Bender et al[26] represented VGs as a lateral force, which is a sourced term distributed in VG covered domain. An improvement to this model with regard to the positioning of this force was proposed.[27] Jirásek[28] suggested adding the circulation results from the changed lift directly to flow. Törnblom and Johansson[29] proposed modeling the increased mixing due to the shed vortices statistically through an approximation of the shed vortices within the Reynolds stress transport equations.

Though CFD is able to model the features of VGs, lower-fidelity and efficient engineering-type models are needed for a fast iterative evaluation. Panel model-based method incorporating a viscous–inviscid formulation has become a prevailing approach for fast evaluation of airfoil performance. Drela and Giles[30] demonstrated the applicability of a viscous–inviscid method to the analysis of static transonic and low Reynolds number airfoils. Riziotis and Voutsinas[31] presented a viscous–inviscid coupled panel method for dynamic stall modeling of pitching airfoils at medium-high Reynolds number; Zanon et al[32] extended this work to rotating multiple airfoils (VAWTs). Ramos-García et al[33] expanded a 2D viscous–inviscid model to encompass the 3D rotational effects by integrating the Coriolis and centrifugal forces into the boundary-layer equations.

The simplification of representing VGs in CFD modeling suggests insight into possibilities for modeling VGs in a viscous–inviscid formulation. Kerho and Kramer[34] proposed introducing VG-added mixing into the boundary layer to the inviscid-viscous coupled code Xfoil through modifying the stress transport equation to mimic the behaviors of VGs. Daniele et al[35] suggested a sin-exponential increment instead of a step change in Kerho and Kramer,[34] which was shown a good agreement with experimental results and increased numerical stability. De Tavernier et al[36] further extended Kerho and Kramer's approach[34] by introducing a smooth step function and decay rate to the source strength term to Xfoil.[37]

However, all these work based on viscous–inviscid formulation only consider steady flow. At this level of fidelity, a model that can model the phenomena of VG-equipped airfoils in dynamic stall does not exist. This work aims to build up on a low fidelity unsteady viscous–inviscid model[32] the capability of simulating the dynamic stall of VG-equipped airfoils. This model would facilitate airfoil design through earlier indications of VG performance in separation prevention.

2 | METHOD

2.1 | Viscous–inviscid coupled double wake model

The baseline unsteady double wake viscous–inviscid vortex model was developed in Zanon et al[32] for dynamic stall modeling in VAWTs. The inviscid and visoucs flow effects are coupled by solving the governing equations of unsteady potential flow together with the integral boundary layer equations on the surface panels, using a semi-inverse iterative algorithm. The wake is modeled by the "double wake" concept; vortex sheets are shed at both the trailing edge and the separation location.

According to Prandtl's boundary layer theory,[38] the incompressible external flow over a body at high Reynolds numbers can be split into two regions: the boundary layer region where the viscosity is substantial and the region outside this layer where the viscosity is negligible.

In the outer flow region, the viscosity effects are assumed negligible. The Navier–Stokes equations are reduced to Euler equations:

$$\rho\left(\frac{\partial \vec{u}}{\partial t} + \vec{u} \cdot \nabla \vec{u}\right) = -\nabla p \tag{1}$$

In the boundary layer, the viscous effects are not neglibible. The Navier–Stokes equations are simplified into the boundary layer equations[38]:

$$\rho\left(\frac{\partial u_s}{\partial t} + u_s \frac{\partial u_s}{\partial s} + u_n \frac{\partial u_s}{\partial n}\right) = -\frac{\partial p}{\partial s} + \mu \frac{\partial^2 u_s}{\partial^2 n}$$
$$0 = -\frac{\partial p}{\partial n} \tag{2}$$

where $\vec{u}$ and p are the velocity vector and pressure, ρ is the density of the fluids, and s and n represent the curvilinear coordinate along the body surface and its normal, respectively.

Additionally, the continuity equation is required

$$\nabla \cdot \vec{u} = 0 \tag{3}$$

A vortex panel method, including a secondary wake at the separation location, is applied to solve the inviscid flow. The flow in the outer region is assumed incompressible, irrotational, and inviscid. The flow is only governed by the continuity equation and irrotationality requirement under these assumptions. The solution for the governing equations then can be obtained by distributing individual elementary solutions (sources and vortex) on the body surfaces; the velocity field can be calculated using the superposition principle of Green's identity. The elementary distribution of the double-wake vortex model (DW model) for the separated flow at time step k is illustrated in Figure 1. As shown in Figure 1, N_p panels with constant strength of source distribution and two constant strength vorticity distribution were used to approximate the airfoil surface. The newest wake shed at the trailing edge and the separation location are modeled by constant strength vortex segments; the old shed wake are convected to vortex blobs. The separation location is determined by applying a separation and reattachment criterion developed in the previous work,[32] which utilizes the results of the boundary layer equations. This criterion is mainly based on the value of the skin friction coefficient, C_f (flow separates when C_f becomes negative). Additionally, it implements other algorithms to overcome some limitation appearing when a boundary layer transition bubble is present. Further elaboration can be found in the work.[32]

Drela's integral boundary approach[30] for steady flow was chosen to compute the boundary layer flow. Drela's approach starts with the standard formulation for the momentum and kinetic energy shape parameter equations stemming from the mass and momentum conservation laws.
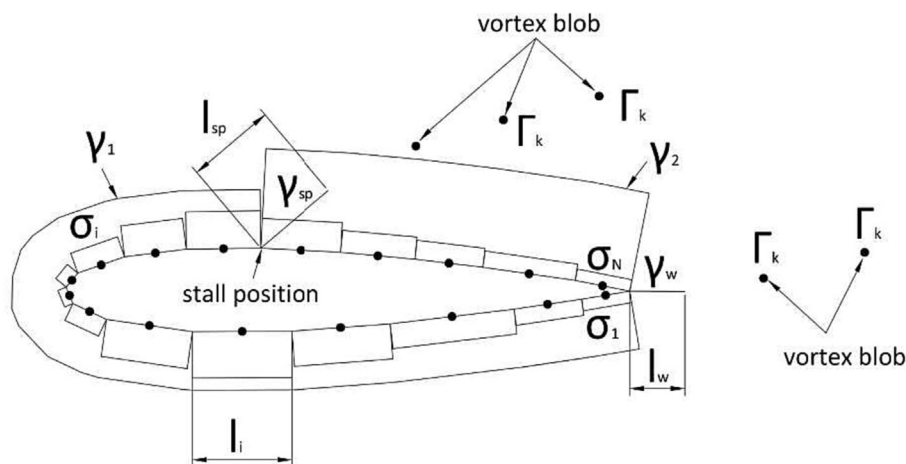

FIGURE 1 Elementary distribution of the double-wake vortex model (DW model) in the separated flow.[32]

$$\frac{\partial(\rho u_s)}{\partial s} + \frac{\partial(\rho u_n)}{\partial n} = 0$$
$$\rho u_s \frac{\partial u_s}{\partial s} + \rho u_n \frac{\partial u_n}{\partial n} = \rho_e u_e \frac{du_e}{ds} + \frac{\partial \tau}{\partial n}$$

(4)

where s and n are the same meaning as in Equation 2, e represents the edge of the boundary layer. τ is the sum of the total shearing and the shear stress.

The first relation given by Drela can be obtained by integrating the momentum equation across the boundary layer.

$$\frac{\xi}{\theta}\frac{d\theta}{d\xi} = \frac{\xi}{\theta}\frac{C_f}{2} - \left(\frac{\delta^*}{\theta} + 2 - M_e^2\right)\frac{\xi}{u_e}\frac{du_e}{d\xi}$$

(5)

The second relation is the kinetic energy integral equation. By multiplying the momentum by velocity, a kinetic energy equation is obtained and integrated across the boundary layer, resulting in the following:

$$\frac{\xi}{\theta^*}\frac{d\theta^*}{d\xi} = \frac{\xi}{\theta^*}2C_D - \left(\frac{2\delta^{**}}{\theta^*} + 3 - M_e^2\right)\frac{\xi}{u_e}\frac{du_e}{d\xi}$$

(6)

where

ξ is the streamwise coordinate

$\theta = \int_0^\infty \left(1 - \frac{u_s}{u_e}\right)\frac{\rho u_s}{\rho_e u_e}dn$ is the momentum thickness

$\delta^* = \int_0^\infty \left(1 - \frac{\rho u_s}{\rho_e u_e}\right)dn$ is the displacement thickness

$C_f = \frac{2}{\rho_e u_e^2}\tau_w$ is the skin friction coefficient

M_e is the Mach number at the edge of the boundary layer

$\theta^* = \int_0^\infty \left(1 - \left(\frac{u_s}{u_e}\right)^2\right)\frac{\rho u_s}{\rho_e u_e}dn$ is the kinetic energy thickness

$\delta^{**} = \int_0^\infty \left(1 - \frac{\rho}{\rho_e}\right)\frac{u_s}{u_e}dn$ is the density thickness

$C_D = \frac{1}{\rho_e(u_e)^3}\int_0^\infty \tau\frac{\partial u_s}{\partial n}dn$ is the dissipation coefficient.

The relations developed are applicable for the laminar and turbulent boundary layer, with different closure relations for each case. This method accurately simulates the entire boundary layer and has been relied on heavily for obtaining airfoil polars in the well-known vortex panel model XFOIL.[37] Its application within the panel method has shown to be robust.

Notably, the viscous–inviscid model is based on the quasi-steady flow approximation for the boundary layer, which has been shown to be a reasonable choice for a comparatively slow aerofoil motion, when reduced frequency (k, definition is given in section 2.4) is smaller than 0.15.[32]

After the solutions for the inviscid and viscous regions are obtained separately, they need to be combined to represent the single flow over the airfoil. The current model introduced a coupling term—transpiration velocity to represent the change on the outer flow due to the presence of the airfoil. The baseline model has been validated for clean airfoils in steady condition and in dynamic stall[32]; more details regarding the development and validation of the baseline double wake model can be found there.

2.2 | VG functionality

The source-term approach proposed by Kerho and Kramer[34] to mimic VGs effects through an artificial increase in mixing at the VG location has show promise results. However, it has the limitation of the simplified nature of the shear term and the calibration for a single VG configuration. De Tavernier et al[36] extended this method for a broader application by proposing a semi-empirical relation between the source term, VG variables and boundary layer properties using a broad range of experimental and high-fidelity numerical data. The source-term integral (I_{ST}) was discovered to be subject to the most influence of VG effects. The following formula was fitting using the reference dataset:

$$I_{ST} = C_0 \cdot \left(\frac{h_{VG}^*}{l_{VG}^*}\right)^{C_1} \cdot \left(l_{VG}^* \cdot \sin\beta_{VG}\right)^{C_2} \cdot \left(U_{VG}\right)^{C_3} \tag{7}$$

where h_{VG}^*, l_{VG}^*, β_{VG} represent the normalized VG height and VG length and the angle of the VG to the flow, respectively. While the previous three terms are inputs to the model, the final term depends on the boundary layer solution at the VG location, with the U_{VG} representing the boundary layer flow velocity at the height of the VG. This velocity is found at the location of the VG using Swafford's velocity profile formulas.[39] The optimal semi-empirical coefficients are set at $C_0 = 0.0240$, $C_1 = 0.2754$, $C_2 = 0.4507$, and $C_3 = 0.2987$. Notably, these semi-empirical coefficients applied in XFOILVG were calibrated with the target to minimize the error in steady maximum lift and the stall angle. Further calibrating these coefficients in the double wake configuration with available unsteady datasets is a potential avenue for future refinement.

The source-term integral can be determined from the boundary layer solutions by

$$I_{ST} = \int_{\xi_{VG}}^{c} \left(\sigma_{0_{VG}}(\xi - \xi_{VG}) \cdot e^{-\lambda_{VG}(\xi - \xi_{VG})}\right) d\xi \tag{8}$$

As the rest of the variables are known or assumed, the strength term $\sigma_{0_{VG}}$ can be obtained inversely.

$$\sigma_{0_{VG}} = \frac{2/I_{ST}}{\lambda_{VG} \cdot \int_0^1 e^{\lambda_{VG}(\xi - \xi_{VG})} d\left(\frac{\xi}{c}\right)} \tag{9}$$

where ξ_{VG} and c represent the VG's streamwise distance from the leading edge and the chord length, respectively. The strength ($\sigma_{0_{VG}}$) and decay rate (λ_{VG}) of the exponential function define the VG influence by the mixing induced at any streamwise airfoil coordinate. As the VG only affects the turbulent boundary layer, the associated closure equations must be modified to reflect that. Changes in the shear-stress coefficient would achieve the goal of increasing the mixing at the desired location. In the XFOIL formulation, which relies on turbulent flow theory by Green et al,[40] the shear-stress term C_τ is the instantaneous shear-stress coefficient, and the rate at which it changes is

$$\frac{\delta}{C_\tau}\frac{dC_\tau}{d\xi} = 4.2\left(C_{\tau_{eq}}^{1/2} - C_\tau^{1/2}\right) \tag{10}$$

where δ is the boundary layer thickness. This relation exists to simulate the lag in the flow shear-stress, as is observed in real-life conditions. Stresses in the boundary layer respond slowly to changing conditions; thus, adding the VG term directly to the C_τ would bypass this relation and potentially destabilize the solution. The term to change would therefore be the equilibrium shear-stress coefficient $C_{\tau eq}$, amended by adding the VG-induced mixing term S_{VG}:

$$\sqrt{C_{\tau_{eq}}} = \sqrt{\frac{0.014851H^*(H-1)\left(H-1-\frac{18}{Re_\theta}\right)^2}{(1-U_s)H^3}} + S_{VG} \tag{11}$$

where H and H^* are shape parameter and kinetic energy shape parameter, respectively; Re_θ and U_s are momentum thickness-based Reynolds number and effective outer layer slip velocity, respectively.

The equilibrium shear-stress coefficient is considered a fundamental closure term of boundary layer solvers and is often tuned to obtain better results, as seen in RFOIL.[41] Adding the VG influence at this location would not interfere with any of the preexisting and proven solution methods used in XFOIL, merely changing the constants to reflect the existence of a VG at the location of higher shear stress. A sudden change in the equilibrium shear stress would allow the flow to respond naturally to the change and converge to a stable solution.

The model is implemented in XFOIL and called XFOILVG.[36] Therefore, it is only applicable for steady flow. In current work, the same module is integrated with the unsteady double wake model introduced in Section 2.1.

2.3 | Coupling the VG functionality with the double-wake model

Though the invicid solver is unsteady in the double-wake model, the same steady boundary layer solver as in Xfoil is used. VG functionality is implemented in Xfoil by adding a dedicated module activated during the boundary layer solution at the location of transition and beyond.[36] The same principle applies to the double-wake model. Firstly, the strength of the exponential VG source-term is calculated and then it determined the VG influence at any streamwise coordinate based on the calculated VG source-term magnitude; this VG term is then added to the equilibrium shear-stress function. Notably, it is assumed for the time being that any VG with a nonzero height in a laminar flow will trigger a transition. From earlier evidence in literature, this assumption is valid for any VG designed to increase the stall angle and maximum C_l. In real-life applications, a VG only works by mixing up the turbulent flow and can trigger transition artificially by inducing instability in the flow. This threshold can be added to the model easily in the future when more knowledge is available about the minimal VG size that can trigger a transition.

TABLE 1 The validation cases.

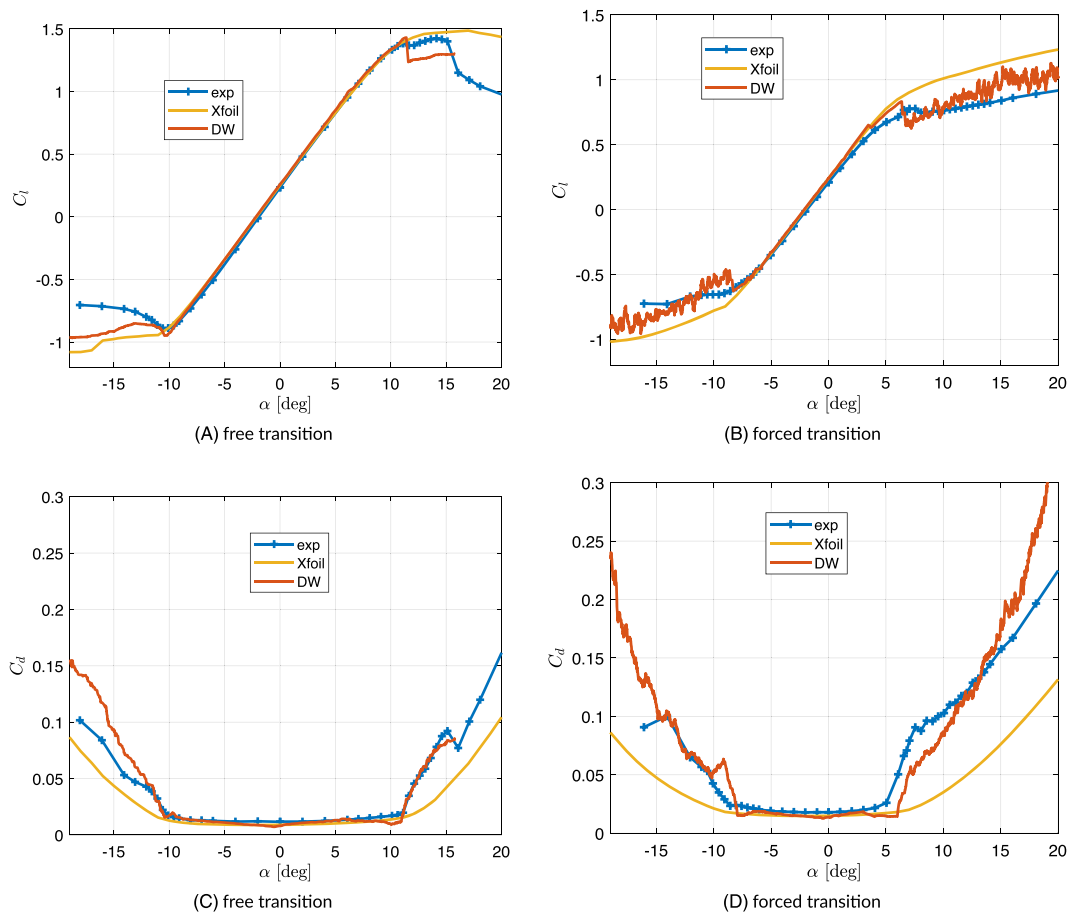| Re $[-]$	Transition	$\alpha_0 [^\circ]$	$A\alpha [^\circ]$	$k [-]$
Steady, 1.0×10^6	Free and forced	-20 to 20	-	-
		-9	7	0.043
Unsteady, 1.0×10^6	Free and forced	1	7	0.043
		11	7	0.043

FIGURE 2 Steady C_l and C_d of clean DU17DBD25 airfoil in free and forced transition.

2.4 | Validation setup

The experimental data[22] are used for the evaluation of the performance of the double-wake model coupled with the VG functionality. The experiment was conducted in the low-speed and low-turbulence (LTT) wind tunnel of Delft University of Technology. This experiment investigated the effect of different types of VGs placed at varying chordwise locations on the lift and drag characteristics of the airfoil DU17DBD25. The resulting data consist of steady polars for the airfoil with and without VGs. It also contains different cases of the airfoil in unsteady pitching motions in both
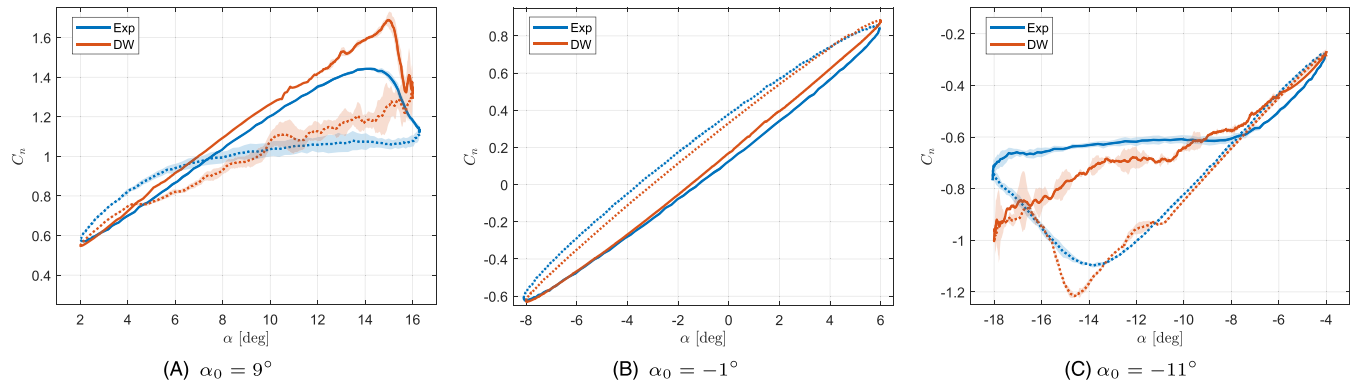

FIGURE 3 Comparison of dynamic C_n between experiments and double-wake vortex model (DW) in free transition for pitching DU17DBD25 airfoil with $A_\alpha = 7°$, k=0.043.
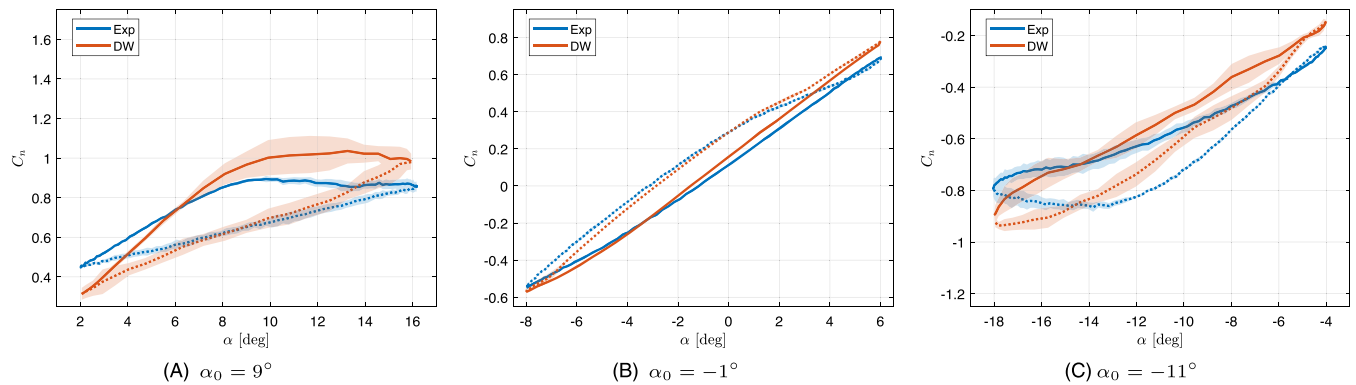

FIGURE 4 Comparison of dynamic C_n between experiments and double-wake vortex model (DW) in forced transition for pitching DU17DBD25 airfoil with $A_\alpha = 7°$, k=0.043.
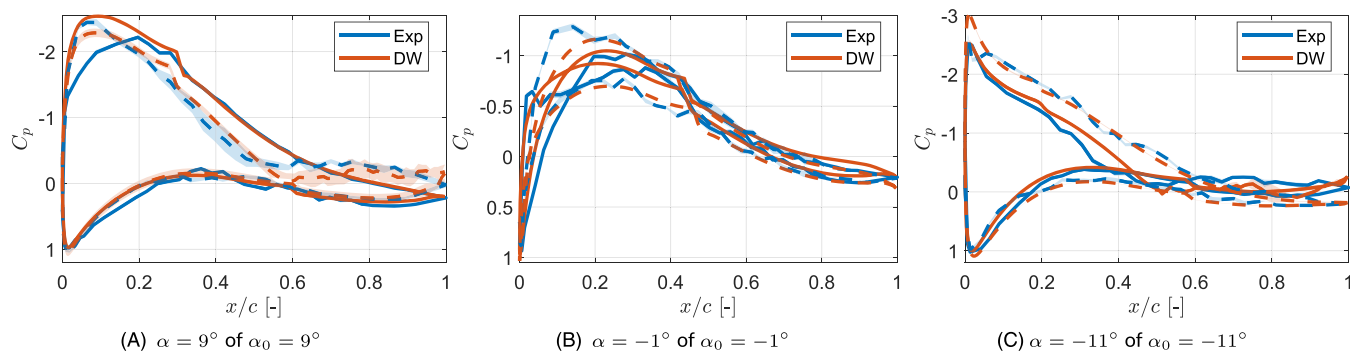

FIGURE 5 Comparison of C_p between experiments and double-wake vortex model (DW) in free transition for pitching DU17DBD25 airfoil; solid line: upstroke; dashed line: downstroke.

attached and separated flow regions. The chordwise VG placement locations and two VG sizes constitute the dependent variables in this experiment. The first VG setup (referred to as VG1) consists of two counter-rotating triangular vane-type VGs of height $h_{VG} = 6$ mm, length $l_{VG} = 18$ mm, and an angle of $\beta_{VG} = 15°$. The intervane distance of VG1 is $d_{VG} = 21$ mm, and the interpair distance is $D_{VG} = 42$ mm. The second VG setup (VG2) has the same shape; however, every dimension, excluding β_{VG}, has been scaled down by a factor of 1.5. Three chordwise VG placement, $x/c = 0.2, 0.3, 0.4$, were tested.

The experiment examined flow in free and forced transition. In the latter case, a zig-zag tape with a thickness of $t = 0.2$ mm was used to force the transition at $x/c = 0.05$ near the airfoil's leading edge at both the suction and pressure sides. Lastly, setting the airfoil to angles of attack in the range of $\alpha = -25°$ to $\alpha = 25°$ provides the steady polars of the airfoil. The experiment defines dynamic pitching cases as an airfoil pitching sinusoidally around a mean angle of attack (α_0), with an amplitude (A_α), and frequency f:

$$\alpha(t) = \alpha_0 + A_\alpha \cdot \sin(2\pi f t) \tag{12}$$

The tested typical reduced frequency k (normalized by $k = \frac{\pi c f}{U_\infty}$) are 0.027 and 0.043.

After a dependency study,[42] the number of panels and the time step are determined to be 239 and the $\delta t = 0.0015$, respectively. The highest unsteady case with a frequency of 1.6 Hz and the corresponding reduced frequency of 0.043, at the Reynolds number(Re) of 1.0×10^6, are selected for the model validation. Kindly note that the initially reported maximum frequency of 2 Hz in the publication[22] has been revised to 1.6 Hz, as disclosed by De Tavernier.[43] The validation cases are summarized in Table 1.

(A) $\alpha = 9°$ of $\alpha_0 = 9°$ **(B)** $\alpha = -1°$ of $\alpha_0 = -1°$ **(C)** $\alpha = -11°$ of $\alpha_0 = -11°$
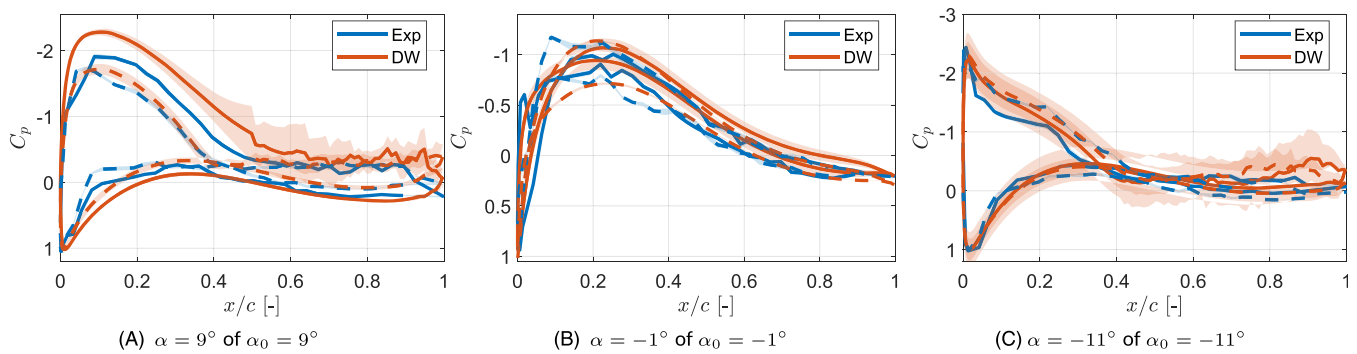
FIGURE 6   Comparison of C_p between experiments and double-wake vortex model (DW) in forced transition for pitching DU17DBD25 airfoil; solid line: upstroke; dashed line: downstroke.
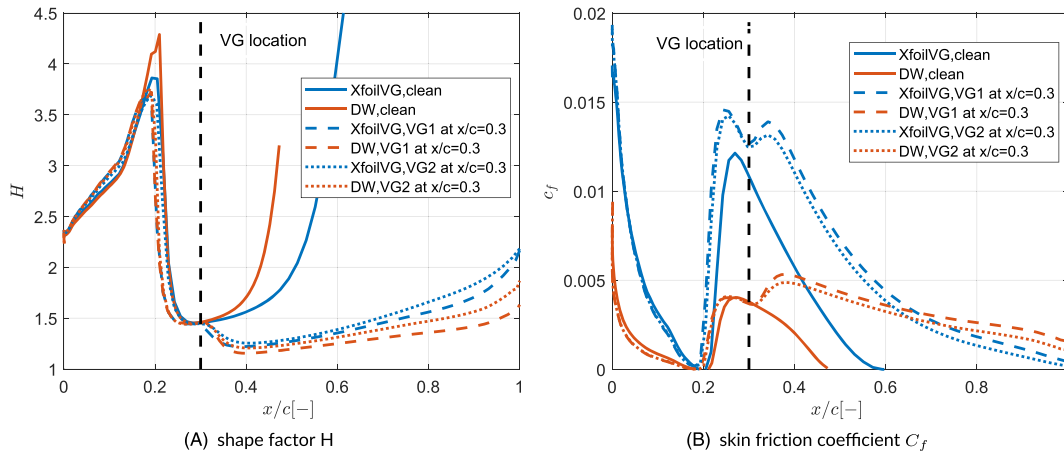

(A) shape factor H   **(B)** skin friction coefficient C_f

FIGURE 7   Comparison of shape factor(H) and skin friction coefficient C_f between double-wake vortex model (DW) and XfoilVG of clean and VG equipped DU17DBD25 airfoil at $\alpha = 14°$ at $Re = 1.0 \times 10^6$.

3 | VALIDATION OF THE DOUBLE WAKE MODEL

3.1 | Validation of a static clean airfoil

Figure 2 compares the steady lift and drag coefficient of the clean DU17DBD25 airfoil obtained by DW with those from Xfoil and measurements at Reynolds numbers of 1.0×10^6 in free and forced transition, respectively.

In free transition, the lift and drag from the DW model are a great match with both experimental results and Xfoil for the linear region of approximately $\alpha \in [-10°, 10°]$. Similarly to the experiment, at the positive stall angle, the lift predicted by the DW drops drastically. However, it stabilizes after the stall angle, while it keeps decreasing in the experiment. According to Xfoil, the stall occurs at a considerably later stage. In the negative stall region, lift predicted by DW model matches the experiments better than Xfoil. In both the positive and negative stall region, drag predicted by DW model is closer to the experimental results than Xfoil. This improvement can be attributed to the incorporation of the double wake formulation in the DW model, which emulates separated flow dynamics better than single wake model.

The lift curve in forced transition is different from that in free transition. With the forced detachment in the boundary layer, no traditional stall is observed in this forced transition case. The lift curve is divided into two linearly increasing parts with different slopes. The positive and negative angles of attack are where the slope changes are around $\alpha = 6°$ and $\alpha = -8°$, respectively. Unlike free transition, DW predicts much closer values of positive and negative slope turning angles and C_l values to experimental data than those from Xfoil. However, the difference in the lift predicted by DW and Xfoil compared with the experimental data in the linear part of forced transition is slightly larger than in free transition. The drag predicted by DW aligns favorably with that of Xfoil within the attached flow region in this forced transition. However, a slightly greater deviation between DW's predictions and experimental results is evident in this forced transition than in free transition. Analogous to the free transition, the DW model significantly enhances the accuracy of drag prediction within the separated flow region when compared to Xfoil.
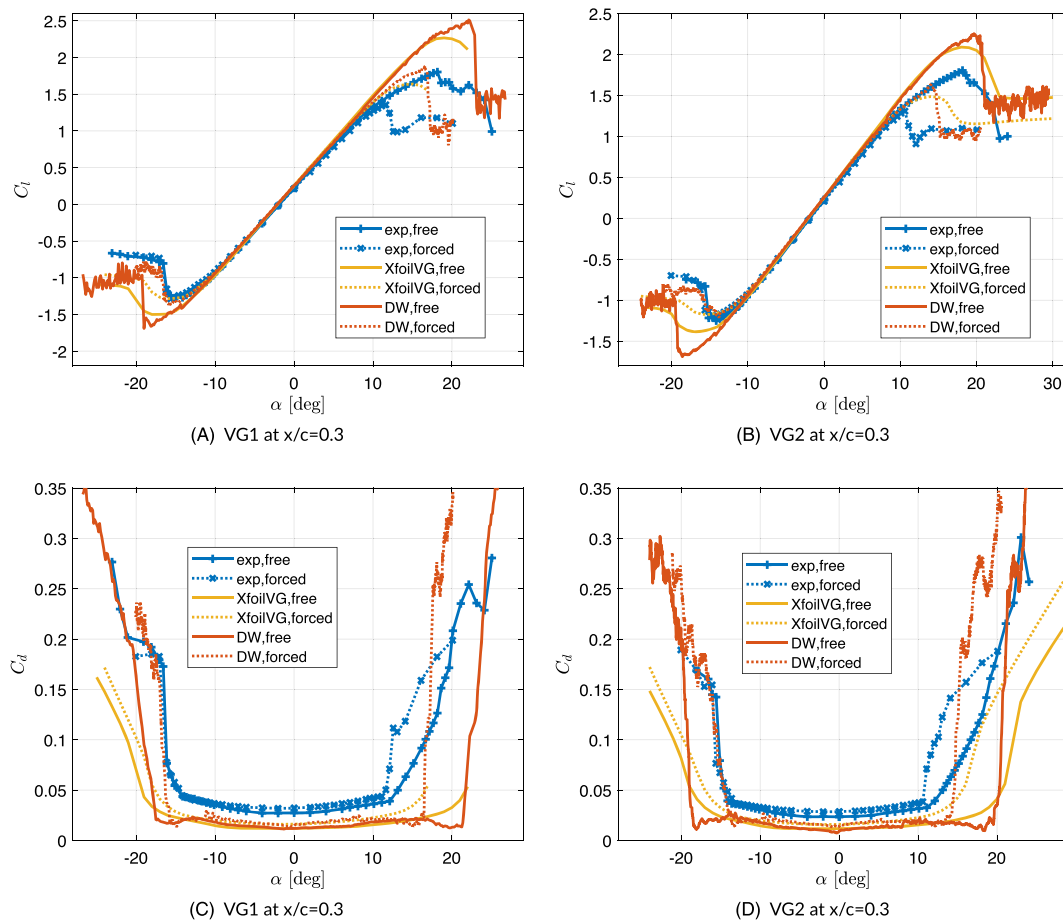

FIGURE 8 Steady C_l and C_d of DU17DBD25 airfoil with VG1 and VG2 located at chord locations of $x/c = 0.3$ in free and forced transition.

3.2 | Validation of a pitching clean airfoil

Figure 3 compares DW against measurements in the dynamic C_n of clean DU17DBD25 airfoil pitching at three different mean angles of $\alpha_0 = 9°, -1°, -11°$ with $A_\alpha = 7°$ at $k = 0.043$ in free transition. The three mean angles of attack represent the positive deep stall region, linear region, and negative deep stall region of the steady polar, respectively. For the unsteady polar, the part of the increasing angle of attack (upstroke or pitch-up motion) and the decreasing angle of attack (downstroke or pitch-down motion) are plotted with solid and dashed lines separately. The standard deviation of three cycles from DW and seven cycles from measurements are represented by the shaded area.

The two curves match reasonably well for $\alpha_0 = -1°$. Despite this, a slight difference in the width and slope of the hysteresis loop exists. The narrower width implies that the phase difference between pitch-up and pitch-down predicted by DW is smaller than that of the experimental data. The difference indicates that the airfoil wake develops to a new state quicker in DW than in the experiment, which is reasonable as the viscous effect of the outer flow where the wake is convected is ignored in the DW. Nonetheless, just as for the steady lift coefficient curve, the model matches experimental data sufficiently close in the linear region of the normal coefficient polar.

For $\alpha_0 = 9°$, the normal coefficient curve in the attached flow during the pitch-up motion matches well with slight overprediction from the DW. The experimental data show an earlier and more gradual decrease in C_n. DW predicts a slightly later but sharper drop in C_n. The earlier decrease in C_n in the experimental data indicates a start of flow separation while the airfoil was still pitching up. The DW model predicts a later flow separation. After the flow separation, the experimental data indicate that the flow reattached at around $\alpha = 7°$, converging towards the regular hysteresis loop seen at lower angles of attack during downstroke. In contrast, DW predicts the reattachment happened at around $\alpha = 4°$, which is later than the measurements.

For $\alpha_0 = -11°$, the normal coefficient curve slope for the attached flow region during the pitch-down motion is captured well by the DW simulation. However, the model is challenged in predicting the flow separation again. Whereas the experimental data show a gradual decrease in C_n magnitude, the simulation shows a rapid increase following a sharper drop. While the experimental data indicate that the normal force slope flattens out after the separation point on the upwards movement, DW predicts an increase in normal force even for the separated part of the
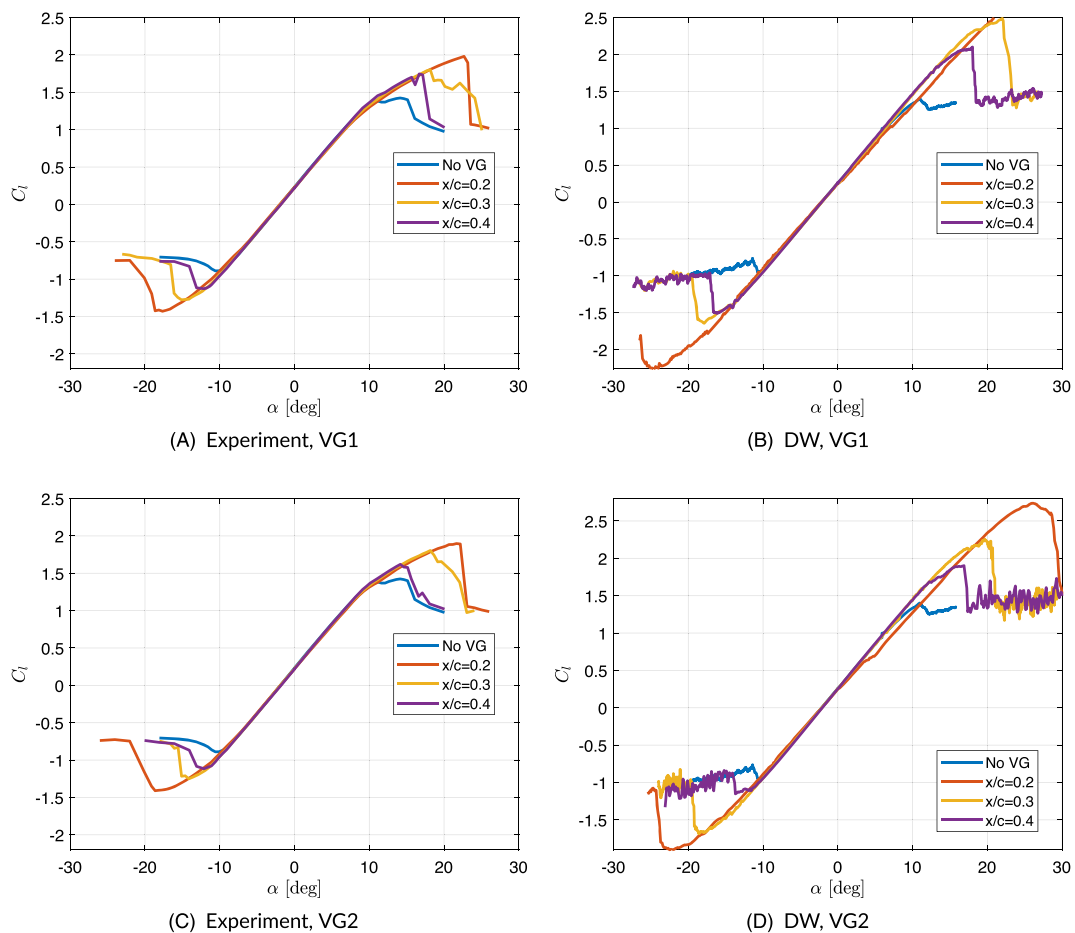

FIGURE 9 Steady C_l of DU17DBD25 airfoil with VG1 and VG2 located at chord locations of $x/c = 0.2$, 0.3, and 0.4 in free transition.

flow. Experiment shows the flow reattachment at $\alpha = -7.5°$, while DW predicts it to happen later at $\alpha = -6°$. A larger standard deviation can be seen in the normal force where the flow experiences separation in both DW and experiments.

The pitching case with mean $\alpha = -1°$ shows minimal noise in C_n values of the three cases. The large-scale dynamic separation of the flow in the other two cases yields much more noise. The stall position is recalculated based on the boundary characteristics at each time step. The geometry of the DU17DBD25 airfoil features a long section of negative slope on the upper side. A sizeable negative pressure gradient, usually seen in thicker airfoils, causes the point to move unpredictably to the sensitive nature of flow separation location calculation. The force calculation in postprocessing includes a term referencing the value of change in pressure; a sudden change to this term over a time step causes massive C_n spikes.

Figure 4 compares the dynamic C_n of the same three pitching motion cases shown in Figure 3 for the transition forced at $x/c = 0.05$. It can be seen in Figure 4B that DW model overpredicts the lift coefficient at the positive angles of attack. This is consistent with the overprediction in steady polar in forced transition in Figure 2.

Though DW can capture the general shape of the unsteady polar, a larger difference from the experimental data can be observed in this forced transition case at $\alpha_0 = 9°$. Compared with the free transition case, the flow is only attached till a smaller angle of $\alpha_0 = 9°$, where the normal force curve increases linearly during the pitch-up motion. Afterward, the flow is fully separated, as indicated by the flattened C_n curve. The C_n curve during the pitch-down motion is also very different from free transition. In free transition, the flow is firstly separated and then starts to reattach again during the downstroke. However, the C_n decreases linearly during the pitch-down motion, which indicates that the flow is not reattached again till the very end of the pitch-down motion due to the forced transition criteria imposed in the model. DW predicts the same trend in the normal force but with relatively steeper slope. Similar to the positive angle, the shape of the unsteady C_n polar predicted by DW resembles that from the experiments well in the case of $\alpha_0 = -11°$, though the slope of C_n hysteresis loop is overpredicted by DW. In free transition, the flow starts with full separation to reattach again during pitch-up motion, while it keeps increasing in forced transition case.

Figures 5 and 6 compare the pressure coefficient C_p between DW and the experimental results for free and forced transition, respectively. The pressure at the mean angles of the three pitching cases are chosen to look into further, that is, $\alpha = 9°$ for $\alpha_0 = 9°$, $\alpha = -1°$ for $\alpha_0 = -1°$, and $\alpha = -11°$ for $\alpha_0 = -11°$. As consistent with the previous discussion, the C_p from DW generally matches well with experimental data in both free
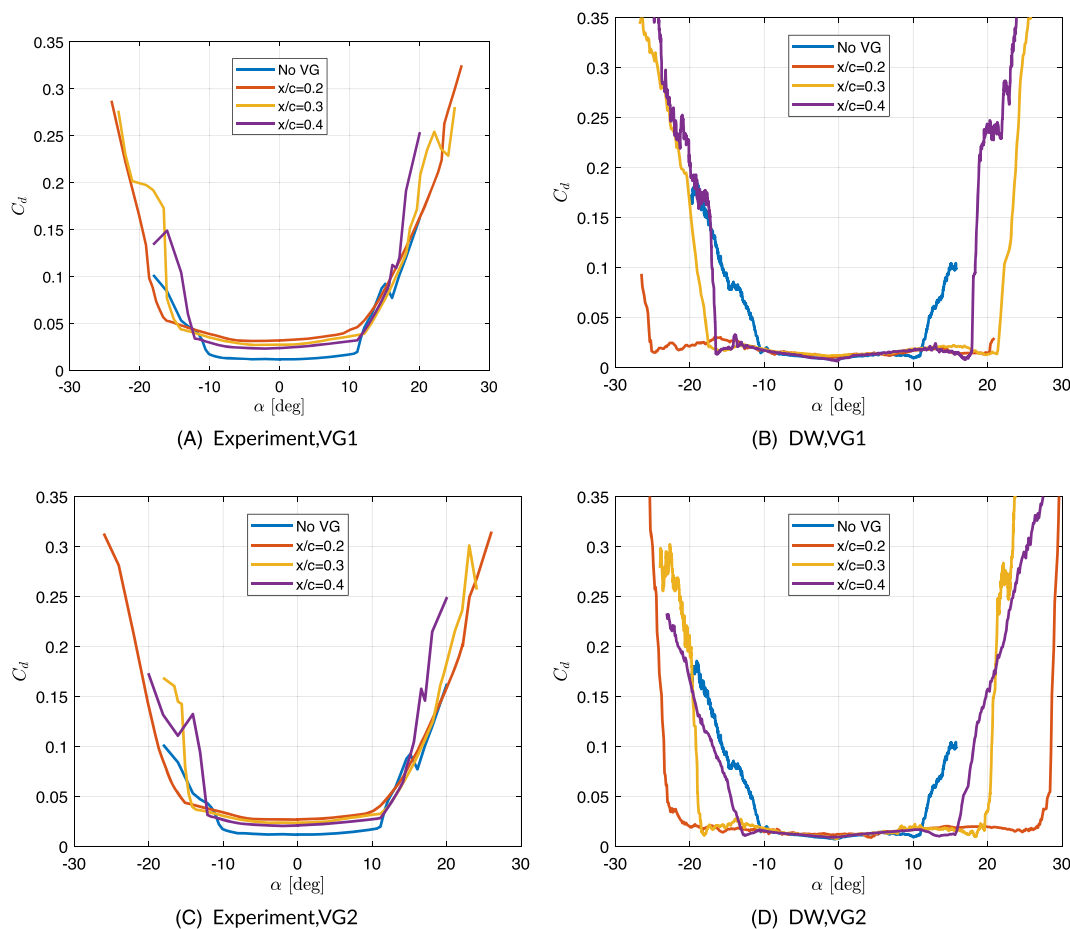

FIGURE 10　Steady C_d of DU17DBD25 airfoil with VG1 and VG2 located at chord locations of $x/c = 0.2$, 0.3, and 0.4 in free transition.

and forced transitions at $\alpha = -1°$, which is within the linear region. The larger discrepancy in C_p in the region $x/c \in [0,0.2]$ between DW and experimental data leads to the disparity in integrated C_n. The difference in this region in the forced transition is reduced. Thereby, the C_n is also in more significant agreement at this angle of attack. For $\alpha = 9°$ of $\alpha_0 = 9°$, DW captured the measured C_p well in both upstroke and downstroke in both free and forced transition. The discrepancy mainly exists in $x/c \in [0,0.2]$ on the pressure side during pitch-up motion in free transition. In forced transition, the discrepancy is within $x/c \in [0,0.5]$. As consistent with the normal force, the flow is fully attached during the upstroke and the flow is separated as indicated by the plateau of constant pressure in $x/c \in [0.5,1.0]$ on the pressure side during the downstroke in free transition. Both DW and measurement show that the flow experiences separation during the upstroke and downstroke in the forced transition. Remarkably, DW captures the separation locations very well in both cases. For $\alpha = -11°$ of $\alpha_0 = -11°$, DW also captures the difference between the upstroke and downstroke and the difference between the free and force transition.

The validation of clean airfoil in pitch motion shows that DW can capture the pressure and the dynamic force generally well, especially for attached flow. The model is challenged to capture the separation and reattachment location accurately, and the forced transition triggered by zigzag tape is also more challenging to model than a clean airfoil.

3.3 | Validation of static airfoil with VG

3.3.1 | Verification of the VG implementation

The implementation of the VG module is first verified against XfoilVG by comparing the boundary layer properties.

Figure 7 compares the shape factor (H) and skin friction coefficient (C_f) between DW and XfoilVG of clean DU17DBD25 airfoil with VG1 and VG2 located at $x/c = 0.3$, at $\alpha = 14°$ and $Re = 1.0 \times 10^6$. As seen in Figure 2, DW shows that the clean airfoil is under stall at this angle of attack. As shown later in Figure 8, the stall is delayed by the application of VG. The flow becomes fully attached at this angle of attack. The shape factor in Figure 7A in all settings rises steadily until a rapid drop caused by a free laminar/turbulent transition at around $x/c = 0.2$. After the drop, the
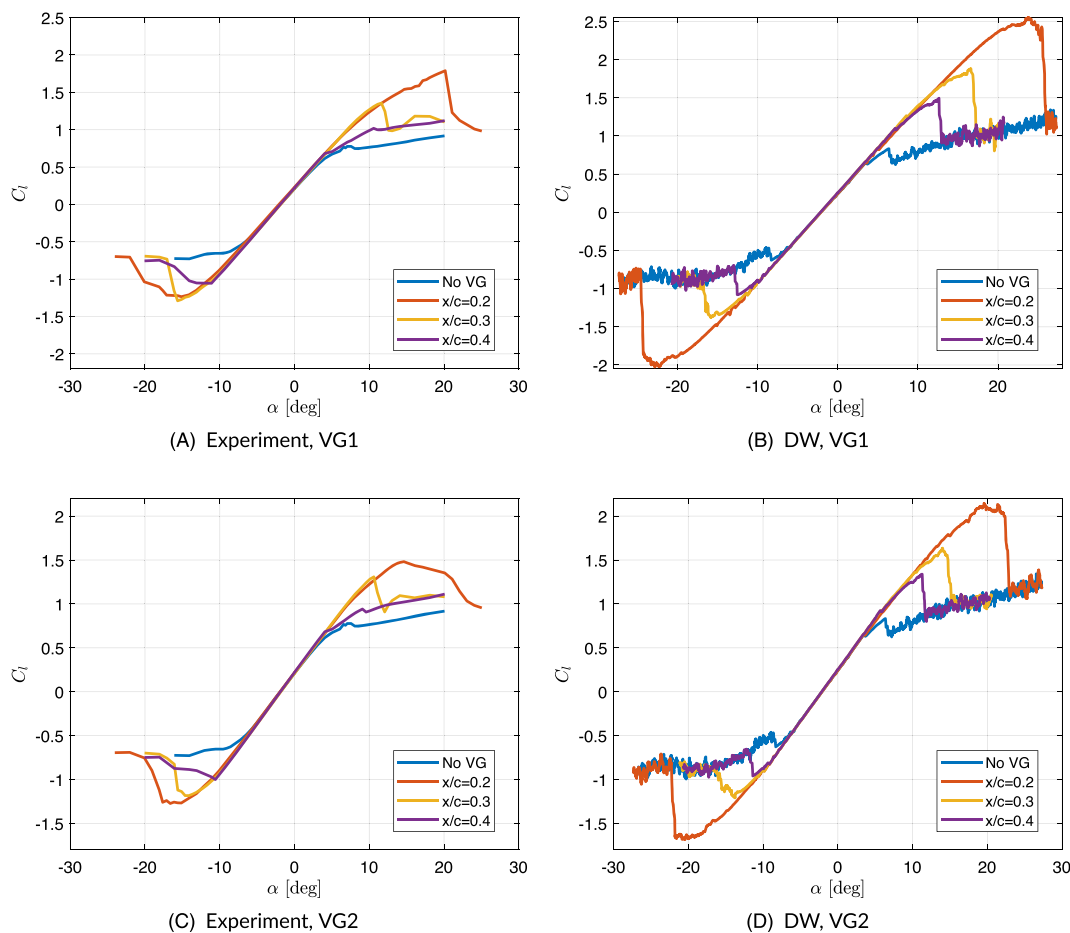

FIGURE 11 Steady C_l of DU17DBD25 airfoil with VG1 and VG2 located at chord locations of $x/c = 0.2$, 0.3, and 0.4 in forced transition.

(A) Experiment,VG1 (B) DW,VG1
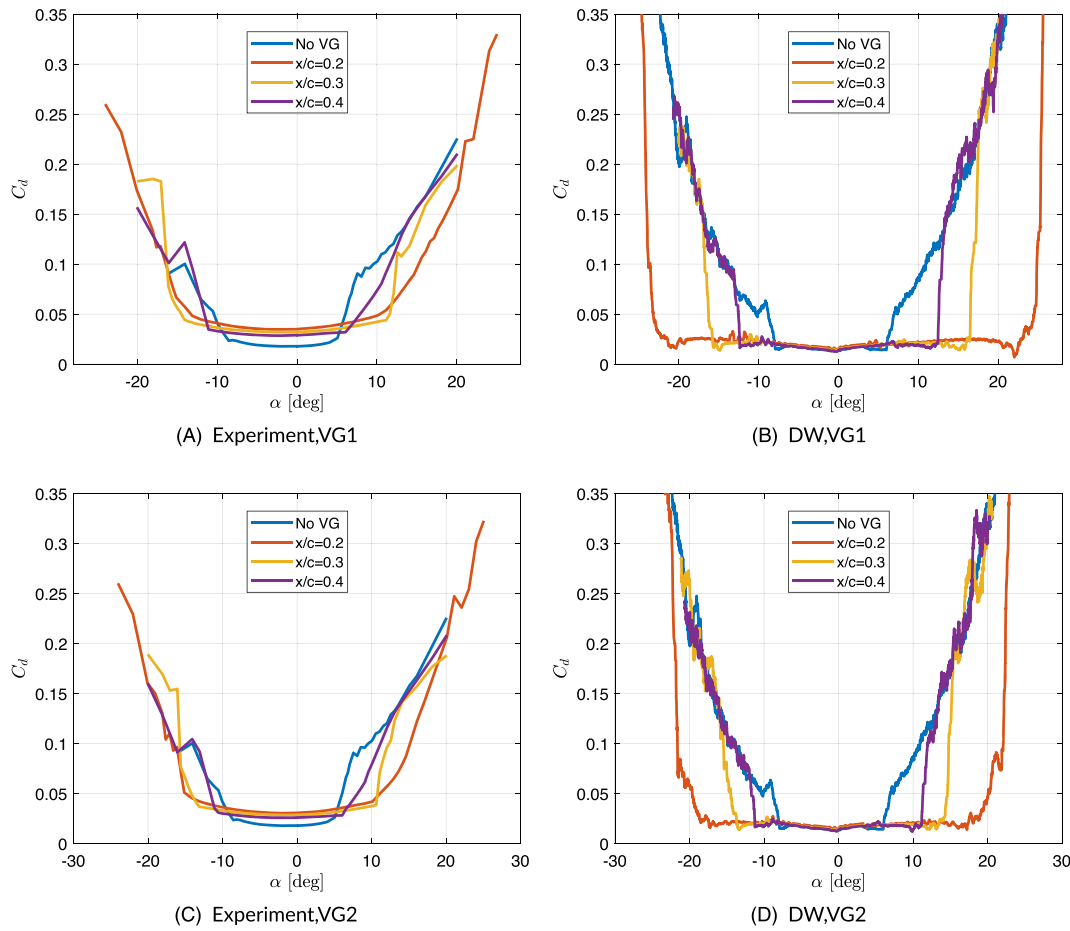
(C) Experiment,VG2 (D) DW,VG2

FIGURE 12 Steady C_d of DU17DBD25 airfoil with VG1 and VG2 located at chord locations of $x/c = 0.2$, 0.3, and 0.4 in forced transition.

TABLE 2 A summary of the positive and negative stall angles and the corresponding C_l from DW and experiments.

VG type	Transition type	VG location	Positive α_{stall}		Negative α_{stall}		max C_l		min C_l	
			Exp	DW	Exp	DW	Exp	DW	Exp	DW
Clean	Free	N/A	15.1	10.9	−10.6	−10.7	1.4	1.4	−0.89	−0.95
	Forced	N/A	7.6	6.4	−9.1	−8.3	0.78	0.83	−0.64	−0.63
VG1		0.2	22.7	>25	−17.7	−24.6	1.98	N/A	−1.43	−2.3
	Free	0.3	18.2	22.1	−15.1	−18.7	1.8	2.5	−1.28	−1.59
		0.4	17.4	18.0	−12.1	−16.6	1.7	2.1	−1.13	−1.49
		0.2	20.1	23.8	−15.1	−22.4	1.79	2.5	−1.24	−2.0
	Forced	0.3	11.6	16.7	−15.6	−16.1	1.36	1.88	−1.29	−1.34
		0.4	10.6	12.6	−11.1	−12.6	1.02	1.49	−1.06	−1.08
VG2		0.2	22.2	26	−18.6	−22	1.89	2.7	−1.41	−1.9
	Free	0.3	18.2	19.7	−14.1	−19.2	1.81	2.2	−1.25	−1.60
		0.4	14.2	16.9	−12.1	−13.7	1.62	1.9	−1.12	−1.15
		0.2	14.6	19.6	−15.1	−22.0	1.48	2.1	−1.27	−1.66
	Forced	0.3	10.6	14.0	−14.6	−13.8	1.31	1.6	−1.18	−1.2
		0.4	9.1	11.3	−10.6	−11.4	0.94	1.33	−1.0	−0.96

Abbreviations: DW, double-wake vortex model; VG, Vortex generator.

shape factor of the clean setup continues rising until separation happens. In the cases with VG1 and VG2 located at $x/c = 0.3$, the shape factor experiences a second sharp drop, and a positive gradient maintains until the trailing edge. The shape factor from DW compares well to that obtained from XFOILVG, though there is an offset due to a difference in stagnation point caused by the separation of the flow in the clean case.

While the implementation of the VG module is identical, the partial stall experienced by the airfoil at this angle of attack results in slight differences between them due to the single-wake (XFOILVG)/double-wake formulation (DW). The effect of VG addition on the shape factor is almost identical in the two models; this effect manifests through separation prevention due to increased mixing beyond the VG location and an earlier laminar turbulent transition resulting from it. VG1 more significantly modifies the shape factor than VG2 due to the larger dimensions of VG1.

It is also essential to examine the skin friction coefficient C_f, on which is the separation criterion based. Figure 7B compares the C_f on the upper side of the airfoil of three settings. The C_f firstly decreases steadily until transition at around $x/c = 0.2$ for all the three settings, before rising to a maximum and falling again. For a clean airfoil, this value continues dropping below zero, exceeding the separation criterion of $C_f < 0$ in a turbulent flow. The cases with VGs show a slowly falling value until the VG location at $x/c = 0.3$, where a second sharp rise in C_f occurs. It continues dropping after the second peak. However, it does not go below zero again till the trailing edge, and therefore, separation is not predicted by these models at this angle of attack. Similar to the shape factor, the larger dimension of VG1 results in a more prominent second peak in C_f than VG2. Both XfoilVG and DW capture this trend. DW model shares the same trend in C_f from Xfoil, though the magnitudes are not the same, due to differences in C_f formulation between XFOIL (single wake) and the double-wake model. The great match in shape factor and the trend of C_f implies the correct implementation of the VG modules in the DW model.

3.3.2 | Validation of static airfoil with VG

Figure 8 compares C_l and C_d of DU17DBD25 airfoil with VG1 and VG2 located at chord locations of x/c=0.3 as an example of free and forced transition obtained by DW with those from XfoilVG and experiments. As in the clean case, DW matches well with XfoilVG and measurements for
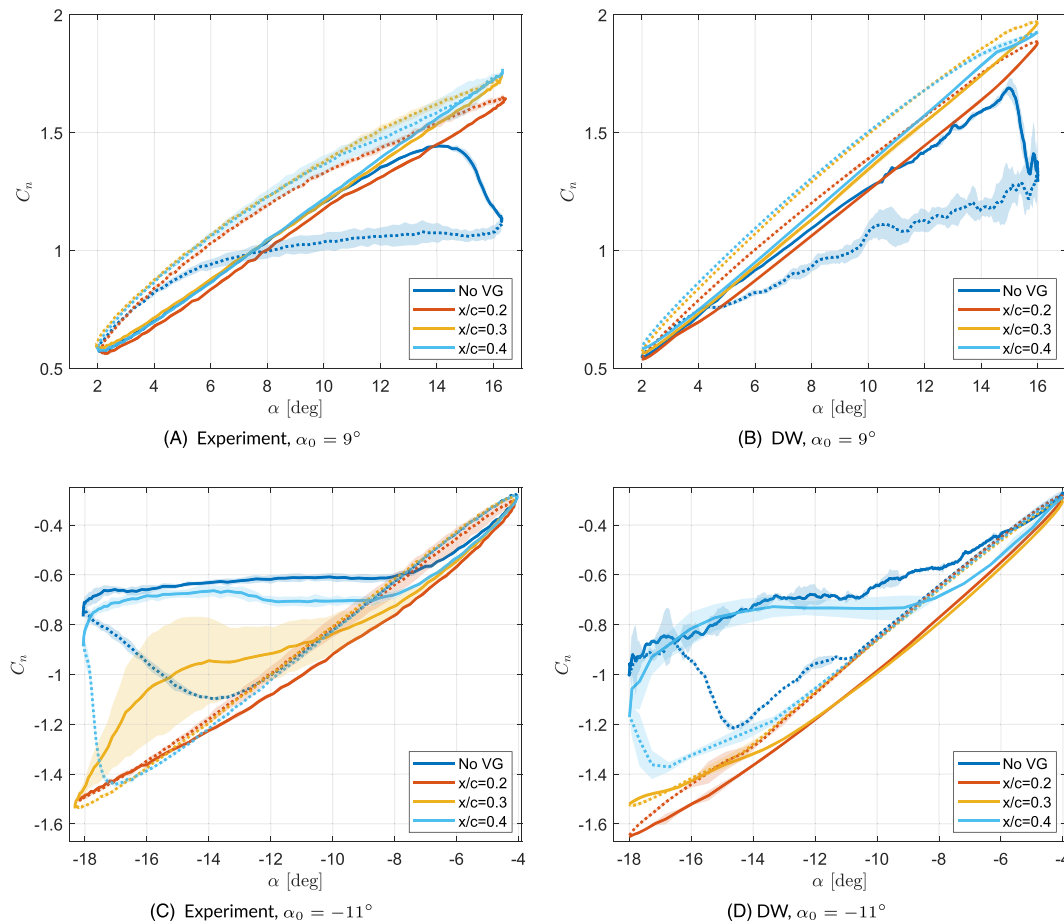

FIGURE 13 Dynamic C_n of pitching DU17DBD25 airfoil with $A_\alpha = 7°$, k=0.043, with VG1 located at chord locations of $x/c = 0.2$, 0.3, and 0.4 in free transition.

the linear part of the lift polar. DW is aligned with XfoilVG in drag prediction for the attached flow region, which is slightly lower than the measured drag value. Notably, in forced transition, DW captures well the measured lift and drag near the negative stall angle. The XfoilVG and DW tend to overpredict the maximal C_l in both clean and VG-equipped airfoils for free and forced transition. DW predicts a sharper lift drop and a steeper drag slope than Xfoil at the positive and negative stall angles in both free and forced transition. DW predicts a closer poststall lift and drag to measurements than XFOILVG in both free and forced transition. This better performance of DW at poststall could benefit from its double wake formulation, which better mimics the real flow in separated cases.

Figures 9 and 10 compare DW and experiments in the steady lift polar of the airfoil equipped with VG1 and VG2 located at $x/c = 0.2, 0.3, 0.4$ in free and forced transition, respectively. The steady polar of the clean airfoil is plotted as a reference. In good agreement with measurements in free transition, the linear part of the polar is extended in both positive and negative angles after VGs are installed. The stall angles increase as VG moves towards the leading edge. In forced transition, no obvious drop in C_l as in the typical stall in the positive stall region was observed in VG located at the most downstream location of $x/c = 0.4$ in the experiments, which is the same as the clean case. The significant drop happens again for VG at the other two locations closer to the leading edge of $x/c = 0.2$ and 0.3. However, DW predicts a typical C_l drop caused by stall for all the VG locations. The same as in the free transition case, the linear parts of the lift curves are extended at both positive and negative angles by all VG configurations.

Figures 11 and 12 provide a comparative analysis between DW predictions and experimental data for the steady drag polar of the airfoil incorporating VG1 and VG2, positioned at $x/c = 0.2, 0.3$, and 0.4 in the free and forced transition scenarios, respectively. The steady drag of the clean airfoil is plotted as a reference. Two principal observations can be gleaned from both figures. Firstly, the attached flow region expands for both positive and negative angles as the VGs move closer to the leading edge, in alignment with the lift behavior. The trend is less visible in the positive angle in the free transition than other regions for the experimental results. Consistent with lift polar, the extension predicted by the DW is larger than that from the experiments. Secondly, the drag experienced within the attached flow region with VG installation surpasses that of the clean airfoil, which indicates that the DW model does not accurately capture the viscous drag caused by the existence of VG. This is anticipated given that the empirical VG function was only calibrated to match the lift of the steady polar, failing to account for the impact of VGs on drag.

Despite the consistent overprediction of the maximal C_l and C_d at high angles, the trend of VG effect in the steady polars predicted by DW matches that from experiments well. The proximity of the VG to the leading edge directly correlates with the extent of suppression observed in
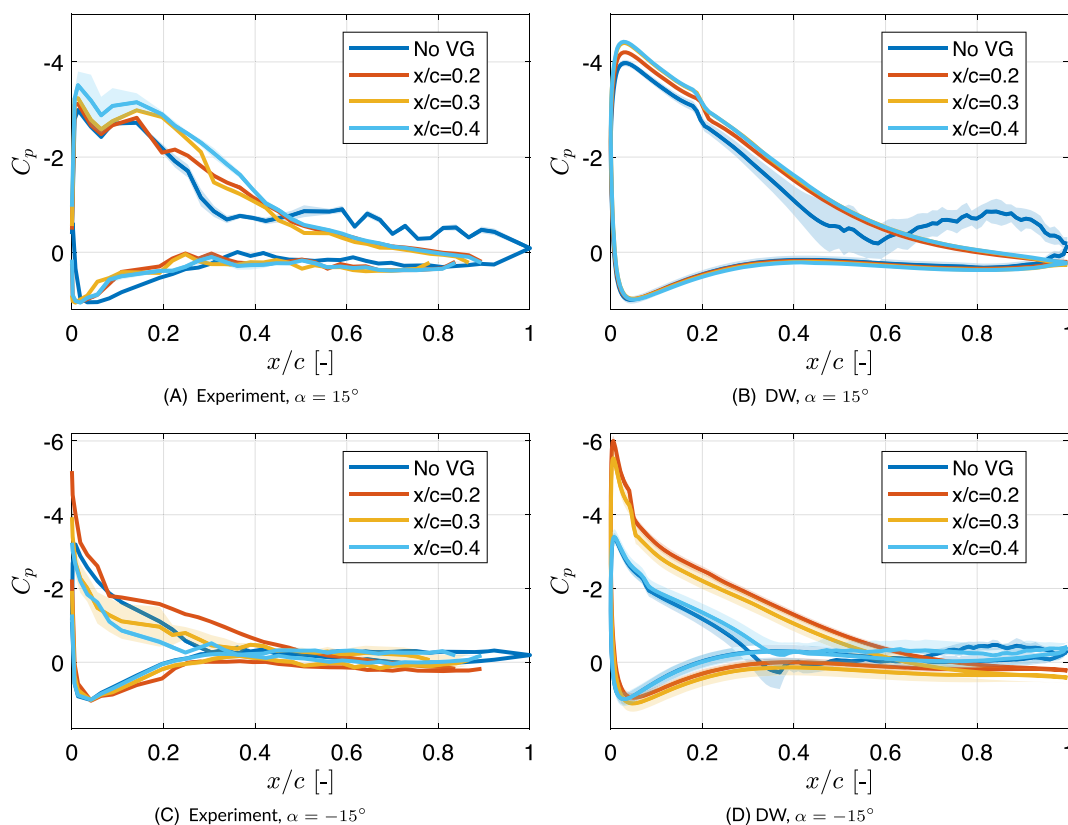

FIGURE 14 Comparison of C_p in upstroke of pitching DU17DBD25 airfoil with $A_\alpha = 7°$, $k=0.043$, with VG1 located at chord locations of $x/c = 0.2$, 0.3, and 0.4 in free transition.

flow separation. VG1 has a larger size than VG2, which results in a larger delay in stall. The capabilities to capture these features show that DW is able to predict the steady effects of VGs.

The comparison of the positive and negative stall angles and the corresponding C_l between the experiments and DW are summarized in Table 2. As seen, both the positive and negative stall angles predicted by DW are larger than those from measurements for the majority of cases. The maximal C_l predicted by DW is also higher. This discrepancy will be present in the pitching cases.

3.4 | Validation of pitching airfoil with VG

Figures 13 and 14 compare DW with experiments in the dynamic C_n of DU17DBD25 airfoil equipped with VG1 at the three locations of $x/c = 0.2, 0.3, 0.4$ with a mean pitching angles of $\alpha_0 = -11°$ and $\alpha_0 = 9°$ in free and forced transition, respectively. The dynamic C_n of the clean airfoil is plotted as a reference. As the effect of VGs on the normal force curve for the attached flow is very limited, the case with $\alpha_0 = -1°$ is disregarded for the discussion in this section.

In the case of $\alpha_0 = 9°$, the dynamic stall is predicted to be suppressed by VG1 at all three locations by DW. The flow is fully attached, and no dynamic stall is predicted. The C_n varies in the linear region, and the values are higher than that of the clean airfoil case. The more downstream the VG is located, the larger the slope of the C_n during the pitch-up motion predicted by DW. All these features agree with those from the experiments.

In the case of $\alpha_0 = -11°$, there is a larger difference between the different VG locations. Consistent with the experiment, the flow is fully separated for the case VG located at the most downstream location of $x/c = 0.4$, and the separation is fully suppressed and the flow remains fully attached for the case of VG1 located at the most upstream location of $x/c = 0.2$ during the pitch-up motion. For the case of VG1 located at $x/c = 0.3$, the flow is separated beyond $\alpha = -11°$, and it is reattached for the rest angles during pitch-up. However, DW shows that the flow is only about to separate at around $\alpha = -15°$. The higher negative stall angle predicted by DW is consistent with the observation in steady case.

Figures 15 and 16 compare C_p at $\alpha = 15°$ of $\alpha_0 = 9°$ and $\alpha = -15°$ of $\alpha_0 = -11°$ between DW and experiments for upstroke and downstroke, separately. The angles of $\alpha = -15°$ and $\alpha = 15°$ are selected as an example due to the large discrepancy in C_n at these angles. At $\alpha = 15°$ during upstroke in Figure 15, separation starts around $x/c = 0.3$ on the pressure side in the clean airfoil, DW predicts the flow separation at
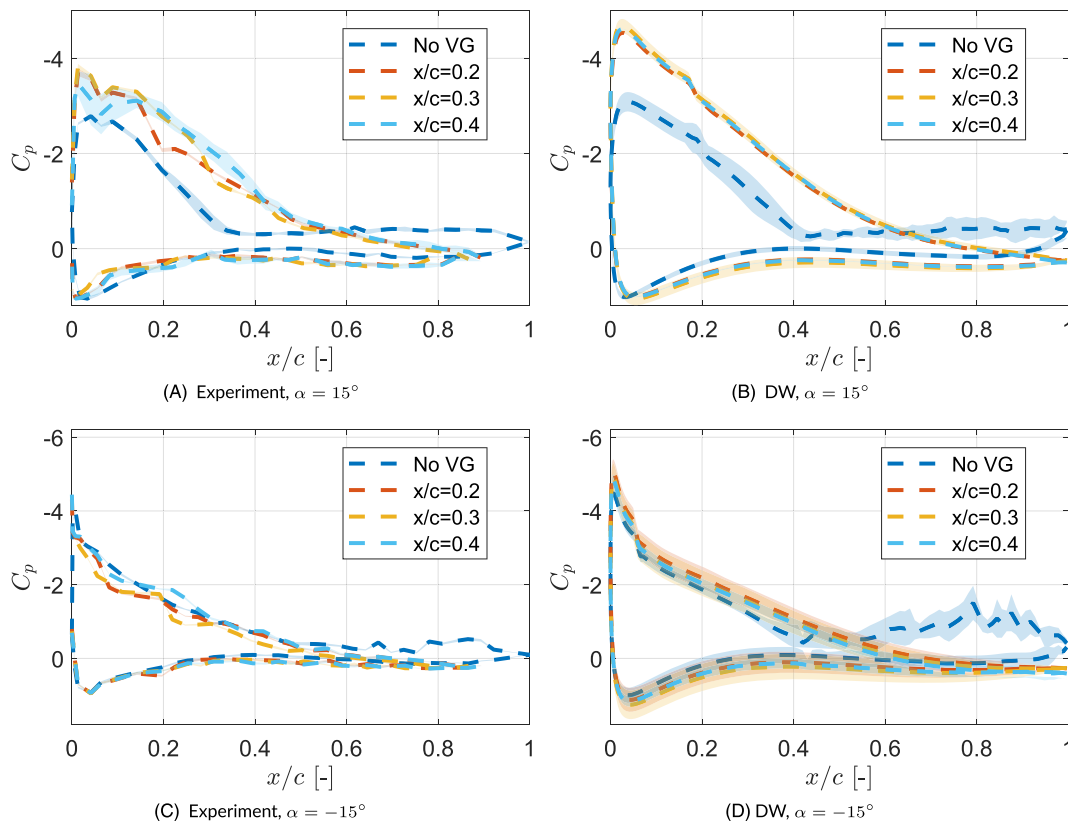

FIGURE 15 Comparison of C_p in downstroke of pitching DU17DBD25 airfoil with $A_\alpha = 7°$, $k=0.043$, with VG1 located at chord locations of $x/c = 0.2, 0.3,$ and 0.4 in free transition.

$x/c = 0.6$. With the addition of VG1 at the three locations, separation is fully prevented, this is well captured by DW models. The further the VG from the leading edge, the higher pressure peaks at the pressure side, this agrees with the measurement. For $\alpha = -15°$, separation is only prevented by VG1 located at $x/c = 0.2$, flow still experience separation for the other two locations in experiment. However, separation only occurs to VG1 at $x/c = 0.4$; it is prevented for the other two locations in DW prediction. This is consistent with the observation in normal force. During downstroke at $\alpha = 15°$ in Figure 16, DW predicts the separation happens at $x/c = 0.4$, which is slightly different from the location of $x/c = 0.3$ indicated by the experiment for the clean airfoil. DW captures the separation location better in downstroke than in upstroke for the no VG case at $\alpha = 15°$. With VG1 installed at all the three locations, the separation is fully prevented, and the pressure magnitude on both sides of the airfoils is increased, which explains the increased C_n during downstroke in VG cases than the clean case. These observations are aligned with the measurements. However, the pressure peak values of DW are higher than measurements; this is consistent with the overall overprediction in normal force from DW at high angles for most of the clean and VG cases. At $\alpha = -15°$, DW agrees with measurements that the flow is separated around $x/c = 0.5$ in clean case, and the flow separation is fully prevented by VG1 at all the three locations during downstroke.

The asymmetry observed between positive and negative angles between Figure 13A,C and between Figures 15 and 16, which is also reflected in the numerical results, is mainly attributed to the significant geometrical upper curvature resulting from the positive camber and the thickness of the airfoil. Conversely, the lower section is flatter. This difference geometry can lead to a different velocity distribution and a different response of placing the VG in the same specific location on the upper and lower sections.

As explained in Section 3.2, the shaded area represents the standard deviation across multiple cycles, which is normally larger for separated flow in comparison to attached flow. As evident in Figure 13B, the presence of VG1 at all three positions effectively mitigates flow separation, resulting in considerably diminished shaded regions across the three VG configurations when contrasted with the clean airfoil shown in Figures 15B and 16B. Regarding the experimental results in Figure 13C, the aerodynamic performance of VG1 located at $x/c = 0.3$ is in between that of VG1 located at $x/c = 0.2$ (completely attached) and that of VG1 located at $x/c = 0.4$ (fully separated),[22] where the flow is the most unstable. This explains the largest amplitude of fluctuation observed in the case of VG1 located at $x/c = 0.3$.
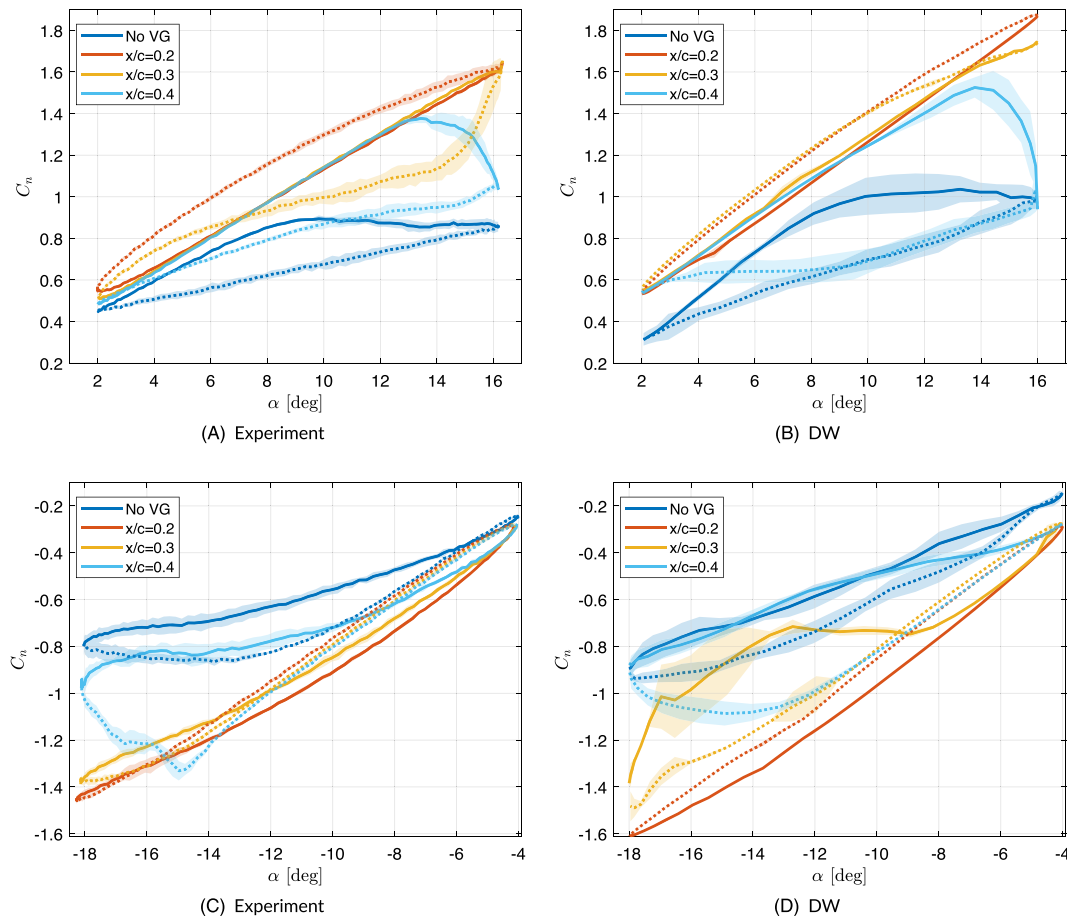

FIGURE 16 Dynamic C_n of pitching DU17DBD25 airfoil with $A_\alpha = 7°$, $k = 0.043$, with VG1 located at chord locations of $x/c = 0.2$, 0.3, and 0.4 in forced transition.

For the more challenging case, VG1 in the forced transition, in Figure 14, the C_n is higher in the cases equipped with VGs than for the clean airfoil for $\alpha_0 = 9°$. The opposite is observed for $\alpha_0 = -11°$. This is corresponding to the extension of the linear lift curve by VGs and the higher lift in the linear part in the steady case in the forced transition. DW predicts a similar trend. Experiments show that the separation in forced transition is more difficult to suppress as the flow still experiences separation for VG1 located at $x/c = 0.3$ and 0.4 and the flow remains fully attached only for VG1 at $x/c = 0.2$, while the flow separation is fully curbed for VG1 at all the three locations in free transition in Figure 13. While DW agrees with experiments generally well for VG1 located at the most upstream and downstream locations, the difference in C_n for VG1 located at $x/c = 0.3$ is larger. Experiment shows partially separation, while DW indicates almost fully attached flow. VGs works even better for the negative stall region in $\alpha_0 = -11°$; the separation of flow of VG1 located at $x/c = 0.3$ is also significantly restrained now in the forced transition in the experiment. However, DW predicts full separation for $x/c = 0.4$ and partially separation for $x/c = 0.3$.

Figures 17 and 18 compare DW with experiment in the dynamic C_n of DU17DBD25 airfoil equipped with VG2 at the three locations with mean pitching angles of $\alpha_0 = -11°$ and $\alpha_0 = 9°$ in free and forced transition, respectively. The C_n of the clean airfoil is also included as a reference. The relatively smaller dimension of VG2 leads to slight difference in dynamic C_n comparing to the airfoil equipped with VG1 in free transition. For the experimental results, the polar of VG2 located at $x/c = 0.2$ and 0.4 does not go back to the polar of full attached flow yet, especially at the large angle of attack for $\alpha_0 = 9°$. While the difference predicted by DW between VG1 and VG2 is small for $\alpha_0 = 9°$.

For $\alpha_0 = -11°$, there is a greater tendency to separate for flow of VG2 located at $x/c = 0.2$. The flow is partially separated beyond $\alpha = -8°$ for VG2 located at $x/c = 0.3$, which happens later at around $\alpha = -12°$ for VG1 in the same configuration. DW also predicts partial separation for flow beyond $\alpha = -11°$ for VG2 locted at $x/c = 0.3$, while the flow separation is fully prevented by VG1 at the same locaiton.

In the forced transition in Figure 18, the flow of VG2 at all the three locations experiences separation with a reduced sepration region when the VG2 location moves towards to the leading edge, while the flow is fullly attached for VG1 at $x/c = 0.2$ for $\alpha_0 = 9°$. DW also predicts slight separation for VG2 at $x/c = 0.3$ above $8°$. For $\alpha_0 = -11°$, similar observation holds. The flow of VG2 at all the three locations experiences partially separation, while VG1 at $x/c = 0.2$ almost curb the separation entirely and the hysteresis of separation of VG1 at $x/c = 0.3$ is much smaller. In DW prediction, the flow of VG2 located at $x/c = 0.2$ is still full attached.
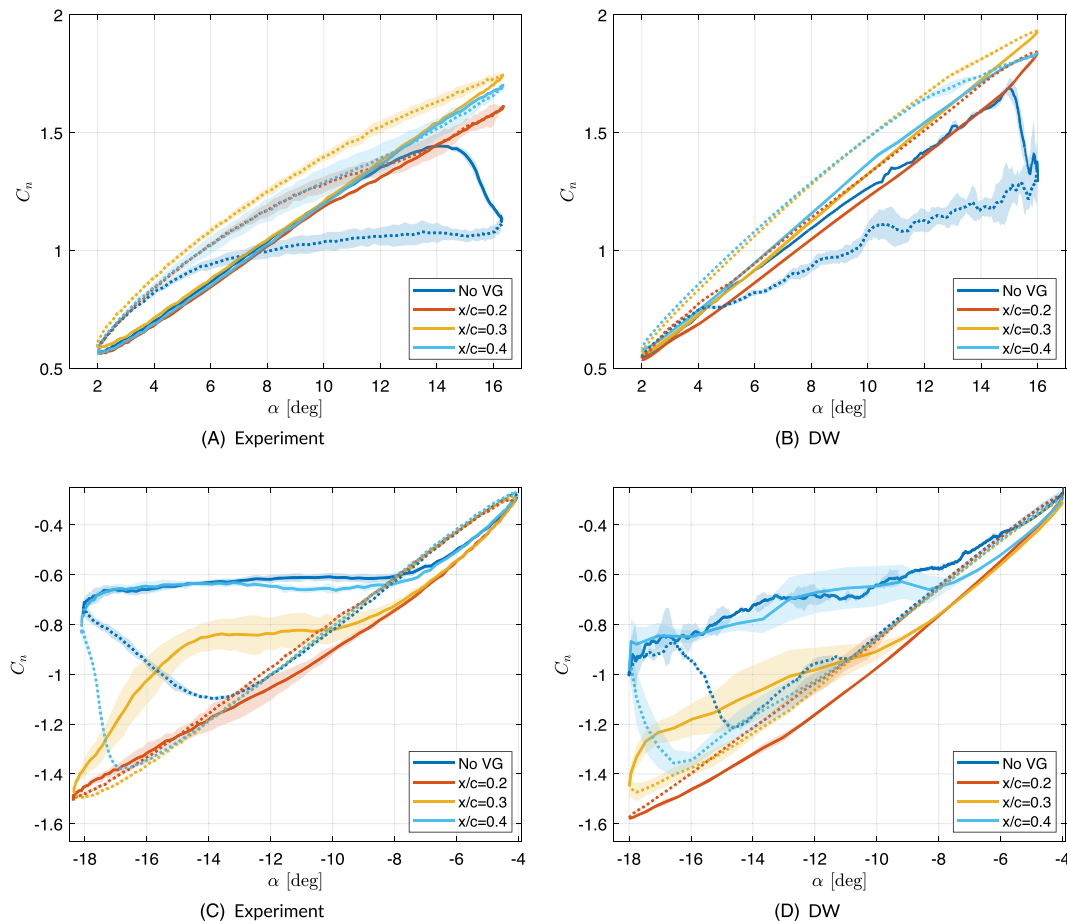

FIGURE 17 Dynamic C_n of pitching DU17DBD25 airfoil with $A_\alpha = 7°$, $k = 0.043$, with VG2 located at chord locations of $x/c = 0.2$, 0.3, and 0.4 in free transition.
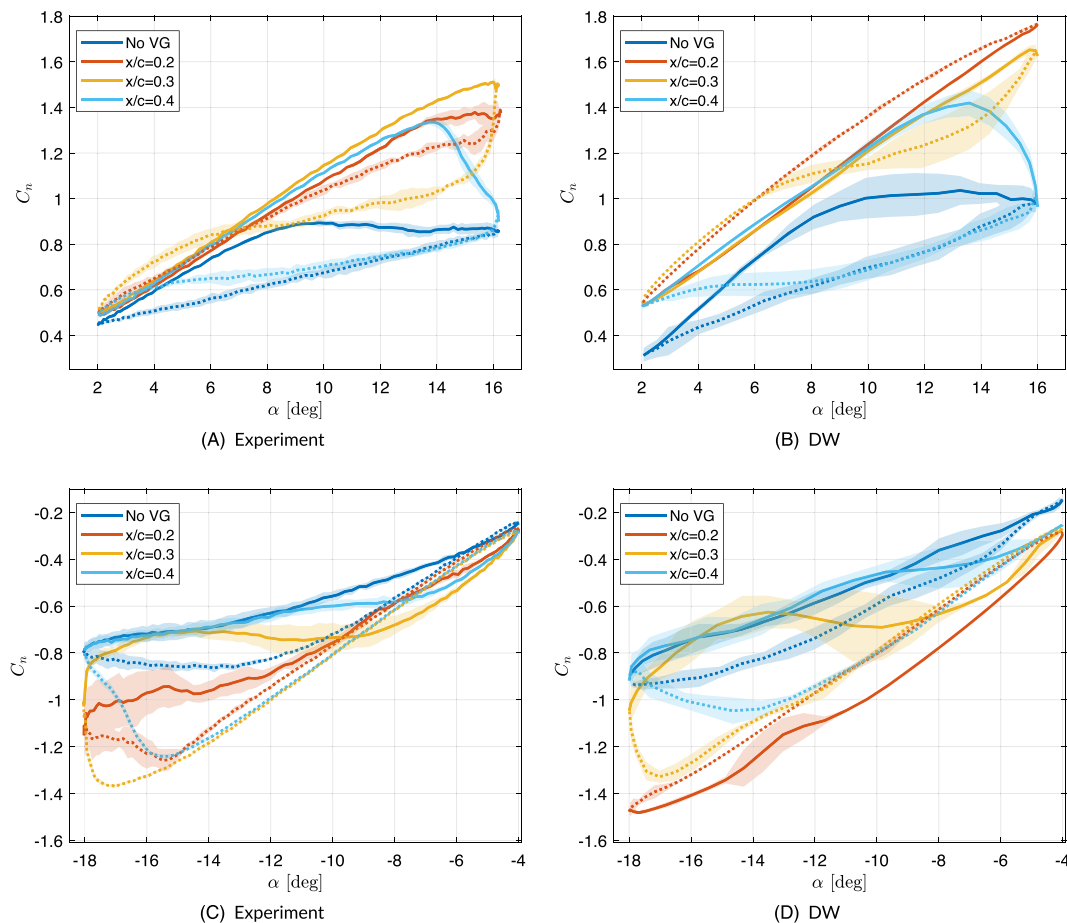
FIGURE 18 Dynamic C_n of pitching DU17DBD25 airfoil with $A_\alpha = 7°$, $k = 0.043$, with VG2 located at chord locations of $x/c = 0.2, 0.3$, and 0.4 in forced transition.

4 | CONCLUSIONS

This work extended an existing double-wake panel models with an artificial mixing source-term VG functionality to predict the dynamic stall of VG-equipped airfoils. The validation of DW shows results with reasonable accuracy compared with experimental data to claim the model's validity, despite the existence of several limitation inherent to this type of modeling approach. For steady cases, despite the overprediction of maximum C_l and stall angle by DW, which is also seen in Xfoil, DW can predict the effects of VG correctly that the linear lift and drag polars got extended and the stall got delayed by VGs. And it can also reflect the effect of different VG sizes and VG chordwise locations. However, the magnitude of the linear polar extension and stall angles are still a significant overestimation by DW. The model predicted a later but sharper stall, indicating that an improvement is needed in the separation criterion affected by the VG. For unsteady pitching cases, DW can capture the difference in normal force between upstroke and downstroke, the difference between the free and forced transition, and the different effects of the different VG sizes generally well. However, the same as in steady cases, DW predicts a latter and sharper stall and a later reattchment in some cases. As such, DW tends to overpredict the VG effect in certain configurations. Overall, the model gives significantly accurate results to claim sufficient validity of the model in a preliminary evaluation of an airfoil's capability to prevent stall with VGs. The relative changes in the results from the different VG configuration to the VG module also allow for a preliminary analysis of desired VGs location and initial sizing.

Despite this, there are several identified limitations in the double-wake vortex-panel method and the VG source-term functionality that can be improved in the future. The semi-empirical VG source-term function in XFOILVG was applied in the model, which is calibrated with the target to minimize the error in steady maximum lift and the stall angle. This can rise error in three aspects. Firstly, Xfoil is based on single wake formulation while DW model consists double wake sheets. Secondly, the VG source-term strength and decay rate can be different in unsteady case than in steady cases. Thirdly, the effect of VGs on drag is not captured. Though the inviscid solution can capture the unsteadiness of the flow, the same quasisteady boundary layer formulation as in XFOIL is assumed for the double wake panel model. The model is challenged when the flow is highly unsteady within the boundary layer. The general difficulties in accurately predicting the occurring moment of the separation and reattachment

and in the forced transition conditions indicate the necessity in improving the transition criteria which needs to reflect the impact of VG or zig-zag tapes on the boundary layer better.

NOMENCLATURE

α angle of attack

α_0 mean angle of attack of pitch motion

A_α angle amplitude of pitch motion

C_l lift coefficient [−]

C_d drag coefficient [−]

C_n normal force coefficient [−]

C_f skin friction coefficient [−]

C_p pressure coefficient [−]

CONFLICT OF INTEREST STATEMENT

The authors declare no potential conflict of interests.

PEER REVIEW

The peer review history for this article is available at https://www.webofscience.com/api/gateway/wos/peer-review/10.1002/we.2889.

DATA AVAILABILITY STATEMENT

Data supporting the findings of this study are available from the corresponding author upon reasonable request.

ORCID

Wei Yu   https://orcid.org/0000-0001-7829-6129

REFERENCES

1. Baldacchino D. Vortex generators for flow separation control wind turbine applications. *Ph.D. Thesis*: Delft University of Technology; 2019.
2. Bak C, Skrzypiński W, Gaunaa M, Villanueva H, Brønnum NF, Kruse EK. Full scale wind turbine test of vortex generators mounted on the entire blade. *J Phys: Conf Ser*. 2016;753(2):22001.
3. Mai H, Dietz G, Geißler W, Richter K, Bosbach J, Richard H, De Groo K. Dynamic stall control by leading edge vortex generators. *J Am Helicopt Soc*. 2006;III:1728-1739.
4. Choudhry A, Arjomandi M, Kelso R. Methods to control dynamic stall for wind turbine applications. *Renew Energy*. 2016;86:26-37. https://doi.org/10.1016/j.renene.2015.07.097
5. Taylor HD. The elimination of diffuser separation by vortex generators. tech. rep., United Aircraft Corporation; 1947.
6. Schubauer GB, Spangenberg WG. Forced mixing in boundary layers. *J Fluid Mech*. 1960;8(1):10-32.
7. Pearcey HH. Introduction to shock-induced separation and its prevention by design and boundary layer control. *Bound Layer Flow Control*. 1961:1166-1344. https://doi.org/10.1016/B978-1-4832-1323-1.50021-X
8. Lögdberg O, Fransson JHM, Alfredsson PH. Streamwise evolution of longitudinal vortices in a turbulent boundary layer. *J Fluid Mech*. 2009;623:27-58.
9. Godard G, Stanislas M. Control of a decelerating boundary layer. Part 1: optimization of passive vortex generators. *Aerosp Sci Technol*. 2006;10(3):181-191.
10. Manolesos M, Voutsinas SG. Experimental investigation of the flow past passive vortex generators on an airfoil experiencing three-dimensional separation. *J Wind Eng Industr Aerodyn*. 2015;142:130-148. https://doi.org/10.1016/j.jweia.2015.03.020
11. Carr L. Progress in analysis and prediction of dynamic stall. *J Aircraft*. 1985;25(1):6-17.
12. Leishman JG, Beddoes TS. A semi-empirical model for dynamic stall. *J Am Helicopt Soc*. 1989;34(3):3-17.
13. Shipley DE, Miller MS, Robinson MC, Luttges MW, Simms DA. Evidence that aerodynamic effects, including dynamic stall, dictate HAWT structure loads and power generation in highly transient time frames. In: Windpower '94; 1994.
14. Allet A, Paraschivoiu I. Viscous flow and dynamic stall effects on vertical-axis wind turbine. *Int J Rotating Machin*. 1995;2(1):1-14.
15. Ferreira CS, van Zuijlen A, Bijl H, van Bussel GJW, van Kuik G. Simulating dynamic stall in a two-dimensional vertical-axis wind turbine: verification and validation with particle image velocimetry data. *Wind Energy*. 2010;13:1-17.
16. Zanon A, Giannattasio P, Ferreira CS. Wake modeling of a VAWT in dynamic stall: impact on the prediction of flow and induction fields. *Wind Energy*. 2015;18:1855-1874.
17. Dyachuk E, Goude A. Simulating dynamic stall effects for vertical axis wind turbines applying a double multiple streamtube model. *Energies*. 2015;8(2):1353-1372.

18. Buchner AJ, Lohry MW, Martinelli L, Soria J, Smits AJ. Dynamic stall in vertical axis wind turbines: comparing experiments and computations. *J Wind Eng Industr Aerodyn*. 2015;146:163-171. https://doi.org/10.1016/j.jweia.2015.09.001

19. Carr L, Mcalister K. The effect of a leading-edge slat on the dynamic stall of an oscillating airfoil. In: Aiaa Aircraft Design, Systems and Technology Meeting. 1983.

20. Choudhry A, Arjomandi M, Kelso R. Methods to control dynamic stall for wind turbine applications. *Renew Energy*. 2016;86:26-37. https://doi.org/10.1016/j.renene.2015.07.097

21. Le Pape A, Costes M, Richez F, Joubert G, David F, Deluc JM. Dynamic stall control using deployable leading-edge vortex generators. *AIAA J*. 2012; 50(10):2135-2145.

22. De Tavernier D, Ferreira C, Viré A, LeBlanc B, Bernardy S. Controlling dynamic stall using vortex generators on a wind turbine airfoil. *Renew Energy*. 2021;172:1194-1211.

23. Velte CM, Hansen MOL, Cavar D. Flow analysis of vortex generators on wing sections by stereoscopic particle image velocimetry measurements. *Environmental Res Lett*. 2008;3(1):15006.

24. Spalart PR, Shur ML, Strelets MK, Travin AK. Direct simulation and RANS modelling of a vortex generator flow. *Flow, Turbul Combust*. 2015;95: 335-350.

25. Zhu C, Chen J, Wu J, Wang T. Dynamic stall control of the wind turbine airfoil via single-row and double-row passive vortex generators. *Energy*. 2019; 189. https://doi.org/10.1016/j.energy.2019.116272

26. Bender EE, Anderson BH, Yagle PJ. Vortex generator modelling for Navier-Stokes codes. In: 3rd Joint ASME/JSME Fluids Engineering Conference; 1999.

27. Jirásek A. Vortex-generator model and its application to flow control. *J Aircraft*. 2005;42(6):1486-1491.

28. Jirásek A. A modified vortex generator model and its application to complex aerodynamic flows. tech. rep., Division of Aeronautics, FFA, FOI-Swedish Defence Research Agency; 2004.

29. Törnblom O, Johansson AV. A Reynolds stress closure description of separation control with vortex generators in a plane asymmetric diffuser. *Phys Fluids*. 2007;19(11).

30. Drela M, Giles MB. Viscous-inviscid analysis of transonic and low Reynolds number airfoils. *AIAA J*. 1987;25(10):1347-1355.

31. Riziotis VA, Voutsinas SG. Dynamic stall modelling on airfoils based on strong viscous-inviscid interaction coupling. *Int J Numer Methods Fluids*. 2008; 56(56):185-208.

32. Zanon A, Giannattasio P, Ferreira CS. A vortex panel model for the simulation of the wake flow past a vertical axis wind turbine in dynamic stall. *Wind Energy*. 2013;16(5):1-20.

33. Ramos-García N, Sørensen JN, Shen WZ. A strong viscous-inviscid interaction model for rotating airfoils. *Wind Energy*. 2014;17:1957-1984.

34. Kerho MF, Kramer BR. Enhanced airfoil design incorporating boundary layer mixing devices. In: 41st Aerospace Sciences Meeting and Exhibit. 2003.

35. Daniele E, Schramm M, Rautmann C, Doosttalab M, Stoevesandt B. An extension of a strong viscous-inviscid coupling method for modeling the effects of vortex generators. *Wind Eng*. 2019;43(2):175-189.

36. De Tavernier D, Baldacchino D, Ferreira C. An integral boundary layer engineering model for vortex generators implemented in XFOIL. *Wind Energy*. 2018;21(10):906-921.

37. Drela M. XFOIL: An analysis and design system for low Reynolds number airfoils. 1989. http://link.springer.com/chapter/10.1007/978-3-642-84010-4_1.

38. Schlichting H, Gersten K. *Boundary-Layer Theory*. 9th. Germany: Springer Nature; 2017.

39. Swafford T. Analytical approximation of two-dimensional separated turbulent boundary-layer velocity profiles. *AIAA J*. 1983;21:923-926.

40. Green JE, Weeks DJ, Brooman JWF. Prediction of turbulent boundary layers and wakes in compressible flow by a lag-entrainment method. tech. rep.; 1977.

41. van Rooij RPJOM. Modification of the boundary layer calculation in RFOIL for improved airfoil stall prediction. IW-96087R, TU Delft; 1996.

42. Bajarūnas LK. Developing a double-wake vortex-panel method model capable of simulating dynamic stall with vortex generators for wind turbine design applications. *Ph.D. Thesis*: Delft University of Technology; 2022.

43. De Tavernier D. Personal communication. 2023.